

# Determinants of Water Permeability through Nanoscopic Hydrophilic Channels

Guillem Portella and Bert L. de Groot\*

Computational Biomolecular Dynamics Group, Max-Planck-Institute for Biophysical Chemistry, 37077 Göttingen, Germany

**ABSTRACT** Naturally occurring pores show a variety of polarities and sizes that are presumably directly linked to their biological function. Many biological channels are selective toward permeants similar or smaller in size than water molecules, and therefore their pores operate in the regime of single-file water pores. Intrinsic factors affecting water permeability through such pores include the channel-membrane match, the structural stability of the channel, the channel geometry and channel-water affinity. We present an extensive molecular dynamics study on the role of the channel geometry and polarity on the water osmotic and diffusive permeability coefficients. We show that the polarity of the naturally occurring peptidic channels is close to optimal for water permeation, and that the water mobility for a wide range of channel polarities is essentially length independent. By systematically varying the geometry and polarity of model hydrophilic pores, based on the fold of gramicidin A, the water density, occupancy, and permeability are studied. Our focus is on the characterization of the transition between different permeation regimes in terms of the structure of water in the pores, the average pore occupancy and the dynamics of the permeating water molecules. We show that a general relationship between osmotic and diffusive water permeability coefficients in the single-file regime accounts for the time averaged pore occupancy, and that the dynamics of the permeating water molecules through narrow non single file channels effectively behaves like independent single-file columns.

## INTRODUCTION

The efficient transport of water through the cell membrane requires special pathways to cross the lipidic low dielectric medium that surrounds cells and organelles. These pathways are provided by proteins embedded in the lipid membrane (1). Water permeation through channels of molecular dimensions is therefore of great interest in biology, but also in technological applications: water-selective pores, such as aquaporins, are suitable as filtering devices (2). Combined with the transport of ions, nanometer size channels are used as sensitive detectors embedded in supported bilayers, with multiple applications such as detection of protein-ligand interaction (3–5) and pH sensors (6). Popular choices for biology inspired pore-based sensing devices are gramicidin A derivatives (7,8), engineered peptidic nanotubes (9–11) and  $\alpha$ -hemolysin (12).

The knowledge of the structure-permeability relationship is an essential prerequisite for the understanding of such narrow channels. Early studies on the relation between osmotic and diffusive permeation through membranes aided the discovery and characterization of water pores in membranes (13). To establish a relation between the measured permeabilities and size of the pore, macroscopic hydrodynamic equations were modified (14,15) to account for the diffusive nature of the permeability coefficients. Such modifications were empirical and ad hoc, rather than based on solid physical theories, and the radii obtained from their applications were regarded as an effective radius or equivalent radius (13) that fitted into that model. The single-file regime was believed to be fully

understood and properly characterized, although recent experiments and computer simulations (16,17) showed deviations from the expected text book model. The theoretical description of the single-file transport showed distinctive diffusive properties (18), like a mean squared displacement proportional to the square root of the time (19–21), but no direct relationship with the size of the pore was put forward.

Studies at atomistic resolution offer a detailed view of the relevant contributions to the channels permeability and selectivity characteristics. Molecular dynamics and Monte Carlo simulations allow us to follow the motions of particles in such microscopic pores. Levitt pioneered the computational study of hard-spheres in a cylindrical pore as a tool to study permeation through narrow pores (22). Recently, more realistic computational strategies modeled the structural and dynamical properties of water in nanoscopic model pores (23–32), with special attention to the newly discovered burst-like permeations in hydrophobic channels, concerted water motion and density distribution patterns. Taking advantage of computer simulations, the electrostatic gating of water channels has also been addressed (33–35). Whereas Beckstein et al. (27,30) devoted much attention to the geometry and polarity of nanopores toward the understanding of the hydrophobic contribution to ion and water gating, the water occupancy rather than the flux was systematically investigated. Similarly, previous work by Allen et al. (23) focused on the structural and diffusive properties of water molecules in nanopores, and a systematic study of their osmotic permeability dependence was not carried out.

We present a systematic molecular dynamics study of channel characteristics that affect water permeability through

Submitted July 9, 2008, and accepted for publication September 22, 2008.

\*Correspondence: bgroot@gwdg.de

Editor: Peter Tieleman.

© 2009 by the Biophysical Society  
0006-3495/09/02/0925/14 \$2.00

doi: 10.1016/j.bpj.2008.09.059

pores of molecular dimensions, and their relation with the liquid structure of the permeating water molecules. The understanding of this relationship yields valuable insights not only in the function of naturally occurring channels, but also for the design of channels with specific properties. To enable a systematic study of the geometrical and electrostatic properties of the pore, we use simplified channels with a helical topology of well defined radius and length, surrounded by a model membrane of controlled thickness. The shape of the channels used in this work is based on the  $\beta$ -helix conformation of gramicidin A in the helical dimer conformation. Designed peptidic channels of increasing length are used to assess the influence of the length at different channel polarities on the water permeability in single-file pores. To study pores with varying radius, we moved away from peptide sequences and, instead, we built chains of pseudo atoms to form the pore walls. The use of helices to model the pore with a finite number of particles (atoms) allows a larger control over the value of the radius for a given height, rise per turn and bond lengths. These systems are used to investigate the radial dependence of the permeability coefficients after the transition from/to the single-file regime. The ratio of osmotic and diffusive permeabilities and its connection with the water pore occupancy is examined for all single-

file and non single-file channels, and implications of these results for the design of new water channels are discussed.

## THEORY AND METHODS

### Design of model channels

Three different D,L polyaniline peptides, of increasing length and based on the  $\beta$ -helix gramicidin A folding motif, were used to study the effect of backbone polarity on the nature of the water transport at different pore lengths. The selected peptides (p-19, p-23, and p-27) span a length similar to that of mini-gramicidin-gramicidin channels (1.7–2.4 nm) (16), and the number of water molecules that can fit in their lumen differ by one between consecutively longer channels. The modeling of the polyaniline peptides was carried out as described previously (17). Soft position restraints (500 kJ/mol/nm<sup>2</sup>) on the peptide backbone and termini capping groups, formyl and ethanolamine, were used to ensure a  $\beta$ -helix fold and a well defined access to the channel. Because a change of the channel sequence would not result in evident and homogeneous changes in polarity, we chose to modulate the polarity of the channels by directly altering the partial charges of the carbonyl groups in the peptidic backbone (Fig. 1 *a*). To this end, the partial charge on the carbon atoms were varied from +0.3 e to +0.6 e in steps of 0.05 e, along with the corresponding opposite charge for the oxygen to guarantee the overall charge neutrality. Because the carbon-oxygen length is fixed by the constraint algorithm, the dipole moment of these carbonyl groups ranges from 1.72 to 3.46 D. The OPLS-AA force-field uses values of +0.5 e and -0.5 e respectively for the carbonyl carbon and oxygen partial charges, which corresponds to a dipole moment of 2.88 D. Because the rest of the partial charges are not changed, the

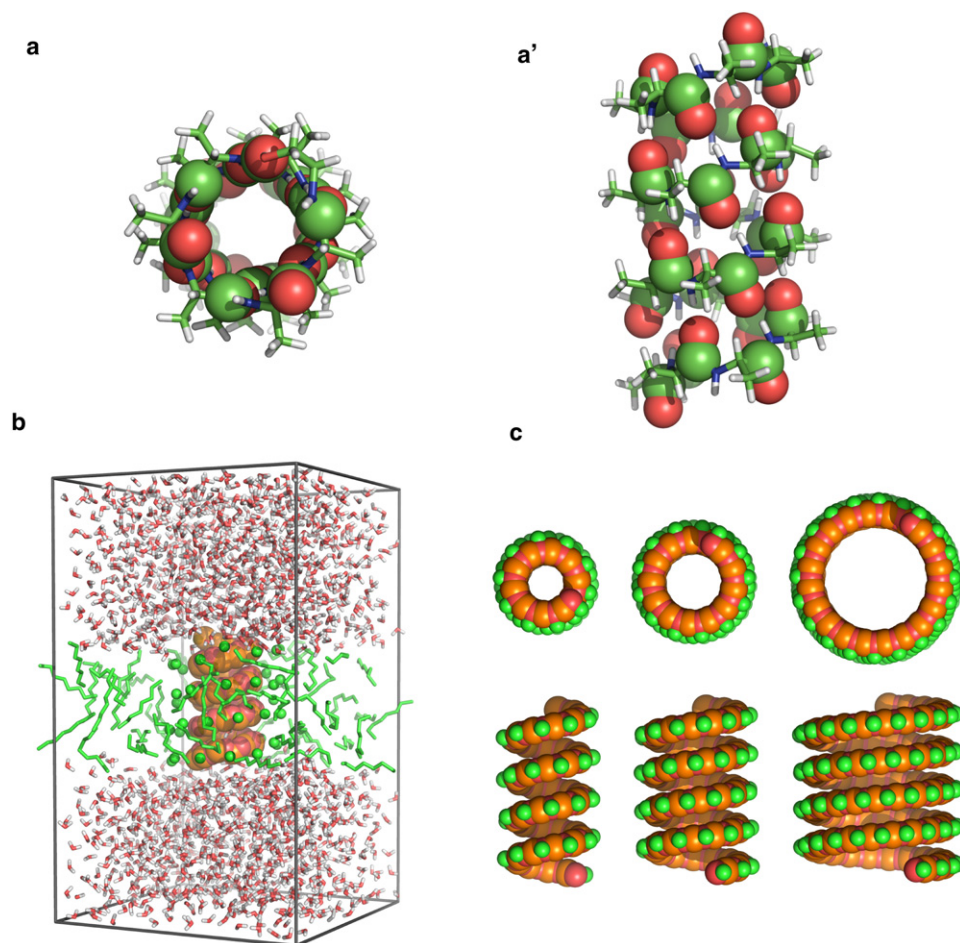


FIGURE 1 Top (*a*) and side view (*a'*) of the polyaniline channel p-23. The positions and alignment of the carbonyl groups is indicated by spheres (carbon atoms, *green*; oxygen, *red*). (*b*) Sketch of a typical simulation box, a system used to study the effect of the radius and polarity is shown. The octane molecules are drawn as sticks and the octane-like atoms connected to the pore as balls. The pore is drawn as balls. (*c*) Top and side view of three designed channels of different radius (from top to bottom: 0.16 nm, 0.30 nm, and 0.55 nm) and length (1.8 nm).

channel remains partially hydrophilic even at low carbonyl dipoles. To ensure that a possible length dependence is solely caused by the channel length and not by possible mismatch between the channel and the membrane, matching membranes were constructed using octane molecules (Fig. 1 *b*). The solvated simulation boxes were prepared using the protocol described previously (17). To obtain initial structures for the channels at different polarities, we started from previously equilibrated initial structures of the channels in their standard OPLS-AA parameters, and we carried out 2 ns molecular dynamics equilibration runs under the new polarity conditions.

The helical chains of pseudo atoms used to study the radial dependence of water permeability were constructed from oxygen-like and carbon-like pseudo atoms, based on the atom types of the carbonyl groups, to mimic the hydrophilic environment of peptidic pores. These pseudo atoms, even in number to build a neutral chain, were arranged alternately and connected with bonds. A slab of octane molecules was used as a membrane. To guarantee a good match with the octane membrane, the helices were surrounded by a second shell of carbon atoms of the same particle type as the octane molecules that form the membrane (Fig. 1, *b* and *c*). The stability of the helix was ensured by using strong position restraints (1000 kJ/mol/nm<sup>2</sup> harmonic force constant) to the initial reference structure of the pore. Nineteen helices of the same length (~1.8 nm) and increasing radius were prepared. The rise-per-turn height was fixed to 0.45 nm, which is similar to the backbone-backbone rise-per-turn distance in gramicidin A in a helical dimer conformation.

The analytical radius of the pore is defined as the distance between a particle of the pore and the center of mass of the pore, and was systematically varied between 0.36 nm and 1.02 nm. The effective radius,  $R_{\text{eff}}$ , and rise-per-turn distance are much smaller due to the volume excluded by the atoms, and due to attractive/repulsive interactions also depends on the charge of the pore. Furthermore, the helical topology imposes a sinusoidal cross-section along the pore. Due to these effects, the effective radially averaged radii used in this study range from 0.13 to 0.57 nm. Each pore of different radius was simulated with seven different pore polarities. The partial charges of the carbon pseudo atoms were increased from +0.3 to +0.6 e in steps of 0.05 e, with a corresponding decrease from -0.3 to -0.6 e for the oxygen pseudo atoms. Series of channels with the same partial charges are named ch-030, ch-035, ch-040, etc. The initial simulation boxes were constructed using the same protocol used for the polyalanine channels.

Interactions between all atoms of the pore and the membrane were described by the OPLS-AA force-field (36,37) (with modified charges for oxygen and carbon as stated previously), and the TIP4P water model (38) was used for the solvent. All simulations were carried out using the GROMACS 3.3.1 simulation software (39,40), with the particle mesh Ewald method (41,42) for long-range electrostatic treatment and a cut-off radius of 1 nm for short-range repulsive and attractive dispersion interactions, modeled via a Lennard-Jones potential. The Settle (43) algorithm was used to constrain bond lengths and angles of water molecules, and LINCS (44) was used for all other bonds and angles, allowing a time step of 2 fs. Short simulations (~300 ps) with anisotropic pressure coupling were run to equilibrate the membrane-pore interface. The temperature in the simulations was kept constant by weakly coupling the channel, octane and water molecules to an external heat bath at 300 K (45). The simulations for production were carried out at constant volume to preserve the integrity of the membrane. For the peptide channels, two sets of 100 ns molecular dynamics simulations with different initial velocities were carried out for each combination of backbone polarity and length. For the helical nonpeptidic channels, each combination of pore radius and pore charge was simulated for 100 ns. Discarding the first nanosecond as equilibration, the complete trajectories were used for all the analysis carried out. Effective pore radii were estimated from time averaged structures extracted from the individual molecular dynamics trajectories using the program HOLE (46). The total simulation time amounted to 17.5  $\mu$ s.

### Radial distribution function of water molecules in the pore

We used the radial distribution function (RDF) to describe the local environment of a reference water molecule in the center of the channel. The radial

distribution function  $g(d)$  is usually defined as  $g(d) = \langle \rho(d) \rangle / \langle \rho \rangle$ , where  $\langle \rho(d) \rangle$  is the density of particles at a distance  $d$  and  $\langle \rho \rangle$  is the system density. To compute the RDF of a water molecule inside the pore, we must first recognize that not all positions are equivalent. To encompass the largest number of particles in the pore, we constrained our analysis to the center of the channel. As reference particles we used the oxygen atom of water molecules located in a section of 0.15 nm in height, positioned at the center of the pore. From those reference particles, all the distances to the rest of the water molecules in the pore are computed. Collecting the number of neighbors at a given radius interval  $\delta d$ , normalized to the appropriate corresponding volume  $\delta V$ , yields  $\langle \rho(d) \rangle$ . To properly account for the restricting geometry of the pore, the normalization volumes were computed as the intersecting volume between a sphere centered at the reference particle and the cylinder defined by the channel. Finally, the densities at distance  $d$  are normalized to the density of unique water molecule pairs inside the channel. Due to the short size of channels and their anisotropy as a system, the radial distribution function does not decay toward the averaged channel density at large distances.

### Permeability coefficients from equilibrium simulations

The mobility of water molecules inside channels of different geometry and polarity was quantified by means of the osmotic and diffusive permeability coefficients (13). The osmotic permeability coefficient,  $p_f$ , relates the net water flux through a channel due to a difference in osmolyte concentration (or equivalently a pressure difference) between the two compartments connected by the channel. It has been shown that it is possible to compute the osmotic permeability coefficient from a simulation under equilibrium conditions by applying rate theory (25,47,48) or a diffusion equation (49) to a collective coordinate describing the transport of one water molecule through the channel. By defining the collective coordinate as the time dependent cumulative displacements of water molecules in the channel, normalized to the channel length, the collective diffusion method proposed by Zhu et al. (49) has the advantage that it does not rely on the single-file regime. We therefore computed the osmotic permeability coefficient as  $p_f = v_w D_n$ , where  $D_n$  is the diffusion coefficient of the collective coordinate previously defined, and  $v_w$  is the molar water volume.

The diffusion permeation coefficient,  $p_d$ , quantifies the equilibrium flux through the channel, and was extracted from the simulations as  $p_d = 1/2\Phi_c v_w$  (17,48), where  $\Phi_c$  is the rate of bidirectional complete water translocations.

The convergence of the permeability coefficients extracted from the simulations was assessed by incremental block averaging. In most of the cases, standard deviations for the whole simulation time were <10% of the computed value. Water-filled pores converge relatively quickly, below 10 ns. Pores of reduced radii (<0.15 nm) and low polarity require longer simulation times, >50 ns.

## RESULTS

### Pore water occupancies and water densities

As previous studies have shown (24,27,30), the most immediate consequence of modulating the pore polarity is the drastic change in pore water occupancy, denoted as  $n$ . Due to the reduction of stabilizing water-pore interactions, the free energy barrier for entering the pore increases as the channels become hydrophobic. To render the measured occupancies comparable among the peptidic pores of different length, we normalized all averaged pore occupancies  $\langle n \rangle$  to the maximum occupancy  $N_{\text{max}}$ . The normalized occupancy is then  $\langle \theta \rangle = \langle n \rangle / N_{\text{max}}$ . Fig. 2 shows the

normalized pore occupancies as a function of the dipole moment of the carbonyl group of the peptidic backbone for the series of polyalanine channels. The results were averaged over two independent trajectories for each backbone polarity and channel length. The normalized pore occupancy is almost insensitive to the length of the pore, with small deviations at low channel polarities. The change in the curvature of the occupancy as a function of the backbone polarity occurs at the same pore polarity for all channels, an indication that the same filling mechanism operates for all the peptidic channels of different length. Note that the occupancy in the pore is not zero for a zero dipole moment of the carbonyl groups. Formally, the appropriate independent variable should be the overall averaged energetic interaction between the pore and the water molecules. In the absence of a pore, implied by the absence of energetic interactions, the occupancy is necessarily zero. Nevertheless, we retain this formulation for convenience.

The observed behavior of the water occupancy can be described by considering an equilibrium between a given number of water molecules in the channel with the total number of water molecules and available positions in the channel. Because there is a large number of water molecules in the surroundings of the pore, we consider the number of bulk water molecules as constant, which appears as a scaling factor in the equilibrium constant (or equivalently, as an additive term in the corresponding free energy). This implies that the ratio of occupied to unoccupied positions are in equilibrium at each combination of length and polarity. The equilibrium constant is given by the difference in thermodynamic potential, which in our case we express in a general form as  $\Delta\Omega(D, f, T, V)$ , where  $D$  is the dipole moment of the carbonyl groups,  $f$  is the fugacity of the water molecules in the surrounding bath,  $T$  is the absolute temperature, and  $V$  is the volume of the channel. The ratio of normalized unoccupied to occupied positions in the channel is

$$\frac{1 - \langle\theta\rangle}{\langle\theta\rangle} = e^{-\beta \Delta\Omega(D, f, T, V)}, \quad (1)$$

that leads to a well known functional form for the normalized occupancy,

$$\langle\theta\rangle = \frac{1}{1 + e^{-\beta \Delta\Omega(D, f, T, V)}}. \quad (2)$$

Equation 2 requires at least a quadratic expression for the free energy as function of the carbonyl dipole moment for the grand canonical potential to reproduce the occupancies obtained from the molecular dynamics simulations (data not shown), implying that the relationship between the free energy and the carbonyl group dipole is not linear.

The time-averaged normalized pore occupancies could either reflect fractions of time in which the pore is fully occupied (24,27), or that just a fraction of the available pore positions are occupied at any given moment. Visual inspection shows that the inner part of the pore is almost empty for low pore polarities, with small fluctuations at the entrance of the pore. Intermittent excursions of clusters of water molecules develop over time, and are virtually always connected to one of the two water compartments. Fig. 3 shows the distribution of the number of water molecules inside the p-27 peptidic channel for different pore polarities. The average size of the cluster depends on the polarity of the pore and correlates with the averaged occupancy: the distribution shifts toward larger clusters as the polarity of the pore increases. At intermediate polarity, the distribution shows a greater variance, illustrating that clusters of different sizes form and disrupt as the water molecules travel through the pore. As the pore occupancy saturates, the single-file column becomes the most stable structure. The OPLS-AA charges lead to a water column that is almost intact, but a small decrease in the charge assigned to the carbonyl group leads to a substantial decrease in the stability of the complete water column. Because

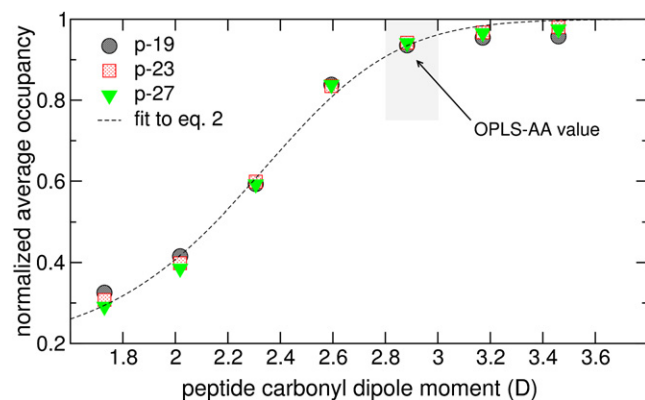


FIGURE 2 Normalized average water occupancy for a series of polyalanine pores as function of the dipole moment of the peptide backbone carbonyl groups. The light gray area indicates the occupancy/dipole moment in the unaltered OPLS-AA force-field. The dashed line indicates the fit to Eq. 2. A quadratic expression for the free energy was employed for the fit to the whole set of data points.

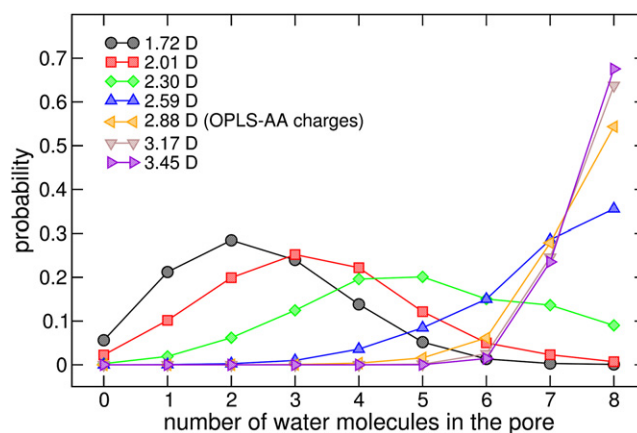


FIGURE 3 Probability distribution of the number of water molecules inside the p-27 peptidic pore for different dipole moments of peptide backbone carbonyl groups.

gramicidin channels are ion channels, and solvation stabilizes the ion in the pore (30,50), the integrity of the water column increases the probability of ion translocation.

The analysis of the pore occupancies as a function of the pore radius and the pore charge can be carried out in analogy with the polyaniline systems of different channel length. However, the maximum occupancy possible for a given channel length changes with increasing radius, and is difficult to estimate from purely geometrical means beyond the single-file regime. Beckstein et al. (27) chose to describe the state of hydrophobic pores as an equilibrium between open or closed states, depending on the water density inside the pore. Because our model helical pores are mainly hydrophilic, the so-called liquid-vapor oscillations are only visible for narrow pores with an effective radius up to 0.16 nm. A two state description, open or closed, would therefore not be discriminative enough. Instead, our analysis of pore occupancies is here carried out based on average occupancies  $\langle n \rangle$  and water densities  $\rho$ , rather than normalized occupancies  $\langle \theta \rangle$ , or the openness of the pore (27). For convenience, the water density inside the pore has been normalized to the bulk water density of the TIP4P water model under the same simulation conditions.

Fig. 4, *a* and *b*, displays the water occupancy and the water density (Fig. 4 *c*) in pores of different radius and polarity. As a general feature for all pore radii, a higher channel polarity results in a higher occupancy of water molecules. At small pore radii,  $<0.15$  nm, the channel is only occupied at high pore polarities (Fig. 4, *inset*). At this range of radii the increase of pore occupancy seems exponential with increasing pore radius. Despite the small set of data points in this region (below 5 in the highest polarity channel), a linear fit to  $\ln \langle n(R) \rangle / L$  for radii smaller than 0.15 nm shows that the correlation coefficient is around 0.99. In this range of small pore radii, and the averaged occupancy reflects time fractions of open/closed states, similar to what was reported for the less polar polyaniline channels and previously in Beckstein et al. (27). The increase ceases after the highest packing configuration is reached, indicated by the first maximum of the density as function of the pore radius (Fig. 4 *c*). For these single-file pores, the maximum of the pore water density occurs when the pores reach a fully occupied single-file (no gaps), corresponding to  $\sim 3.63$  water molecules per nanometer considering a water-water distance of 0.275 nm. The radius at which the density reaches a local maximum depends on the polarity of the pore: more charged pores, with a higher water affinity, reach the fully occupied single-file configuration at a lower radius than less polar pores.

Beyond the optimal single-file packing, the available pore section increases faster than the occupancy. As the channel radius grows, the water molecules start positioning in a helical pattern, that projects along an axial pore plane as a zigzag pattern (Fig. 5 *c*). This structural arrangement of confined water molecules was found previously in pristine single-walled carbon nanotubes (51). Because the new configuration allows only a small additional water occupancy compared to

the volume gained by the increase of the radius, the water density drops. This behavior is due to the discrete nature of water molecules, and it is sketched in Fig. 4 *c*. In this range of radii, we can assume that the occupancy increases linearly with the radius (Fig. 4 *b*), thus the density drops as  $\sim \langle n_{\text{max, singlefile}} \rangle / R_{\text{eff}}^2 + \mathcal{O}(1/R_{\text{eff}})$ . At a radius slightly smaller than the water molecule diameter, a minimum in the occupancy and the density curve occurs: it corresponds to the transition from/to the single-file channel. After this point the helical arrangement of water molecules can no longer be characterized by a no-pass condition. Due to the intrinsic motions of the pore, partially non single file structures can form before the average pore radius exceeds the diameter of a water molecule. As seen from both the channel densities and occupancies, an increase in channel hydrophilicity results in smoother transitions between the two regimes.

The double-file configuration is not a local maximum of the density as a function of the pore radius. Here as well, the density change with respect to the pore radius is more pronounced for the low-polarity pores, e.g., in channel ch-030 there is a transition from double-file to triple-file within  $\sim 0.02$  nm, whereas it requires  $\sim 0.04$  nm for ch-060. After reaching a quadruple-file (at a radius between 0.36 nm and 0.4 nm depending on the polarity) the oscillations in channel density as function of the pore radius damp and converge toward the density of bulk water. After  $\sim 0.4$  nm the water occupancy in channels of different polarity can be approximated by  $\rho_0 V_{\text{ch}}$ , where  $\rho_0$  is the density of bulk water and  $V_{\text{ch}}$  is the available channel volume.

### Structural arrangement of water molecules in the pore

To further illustrate the effect of pore polarity on the occupancy, Fig. 5 *a* displays the normalized radial probability density for a water molecule in pores of the same radius ( $\sim 0.18$  nm) and different polarities. The radially averaged densities, centered at the channel main axis, were also averaged over the length of the pore. The most probable position of a water molecule is located closer to the channel wall the more polar the pore is, a feature also observed in (23). The shift of the most likely position toward the walls of the pore allows the system to fill the channel more efficiently: the overall water density in the channel is higher for the pores with higher charges. For the same reason the transition from and to the single-file regime occurs at a higher pore radius for the low polarity pores: water molecules tend to cluster via hydrogen bonds despite the increase of available area. Because the pore helical shape was constrained to a given length, regardless of the pore radius, they are not fully axially symmetric with respect to the center of mass. In this case the radially averaged density is not a robust criterion to detect the transition from and to single-file regime, but it serves us to observe the effect of pore polarity on the preferred radial distribution for a given radius.

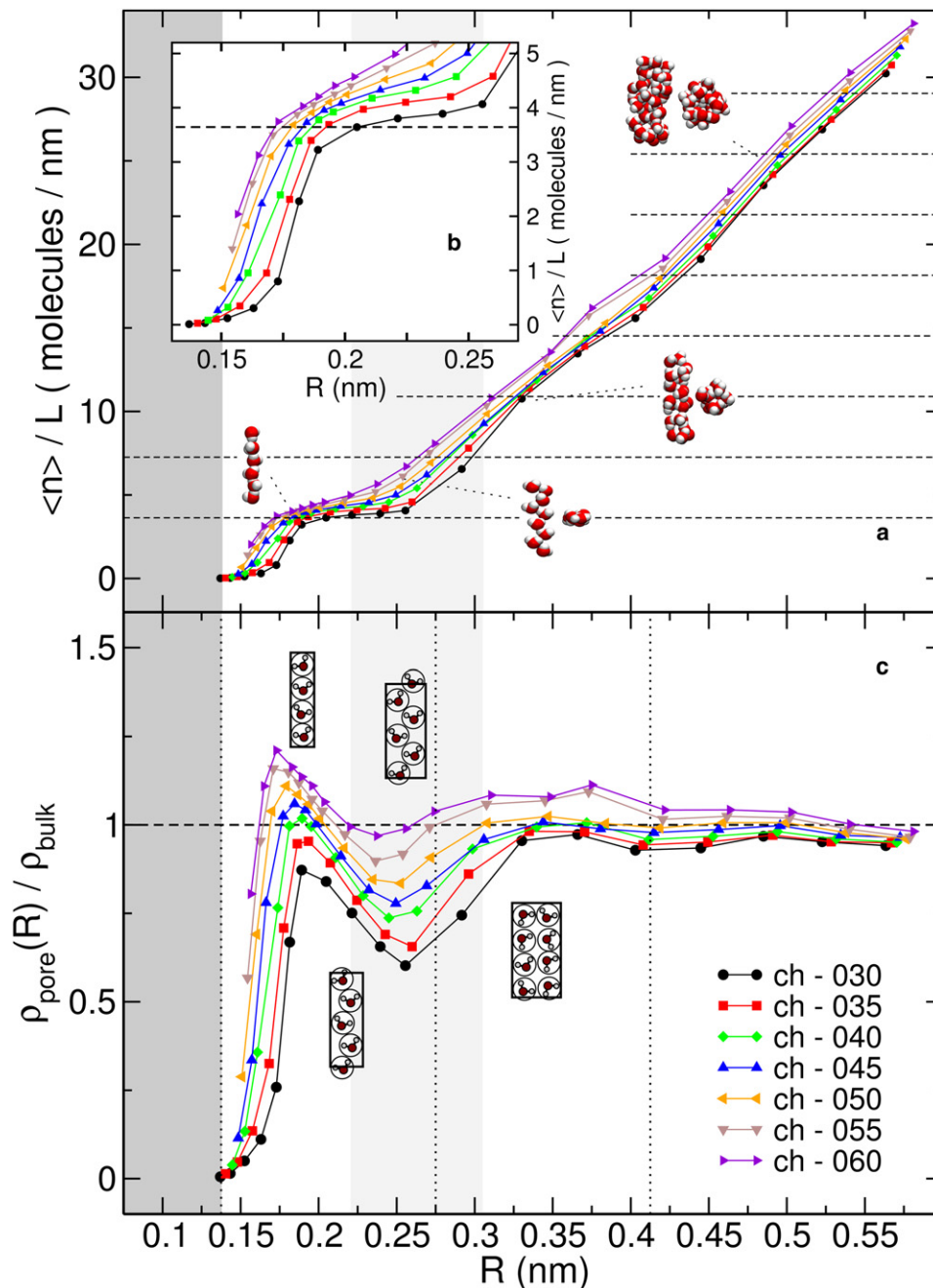


FIGURE 4 (*a* and *b*) Pore water occupancy as a function of the pore radius for different pore polarities. For direct comparison, the water occupancies at each radius were divided by the pore length. The horizontal dashed lines indicate multiples of 3.63 water molecules per nm, the pore occupancy for a perfectly packed single-file. The inset is a detailed view of the occupancies at small pore radius. Several representative snapshots of the water structure inside the channel are drawn, beyond the single file regime both top and side views are displayed. (*c*) Pore water density at different pore radius and pore polarities. The dark gray area indicates a radius smaller than the typical water molecule radius ( $\sim 0.137$  nm), and the light gray area displays the minimum in the water density profile that correlates with the transition from/to the single-file regime. The vertical dashed lines mark the radii corresponding to an integer number of water molecules.

So far, we have described the transition from and to different transport regimes focusing on the channel as a subsystem. To expand the characterization of the transitions, we studied the structural configurations of water in the channels by means of the RDF, or pair distribution function.

Fig. 5 *b* displays the RDF for a water molecule in the pore center for three channel polarities at different radii. The RDF of bulk water, the black dashed curve, is included for comparison. For all RDFs the first peak is located at the same  $d$  value (0.273 nm), which corresponds to the first shell of neighboring water molecules. The red curves show the RDF for the single-file regime of maximum water density. The peak pattern is

characteristic of the single-file regime: each maximum is located at an integer number times the water-water distance. As the channel becomes more polar the height of the first peak increases. This finding is consistent with the higher water densities in polar channels presented in Fig. 4 *c*.

As the radius of the pore increases, the second peak lowers its relative density and moves toward shorter distances, indicating that a zigzag pattern emerges. The green curve is the RDF for the radius previous to the transition, the dashed-dotted curve is the RDF corresponding to the radius at which the density displays a local minimum, i.e., where the transition to a double-file occurs. The magenta curve represents

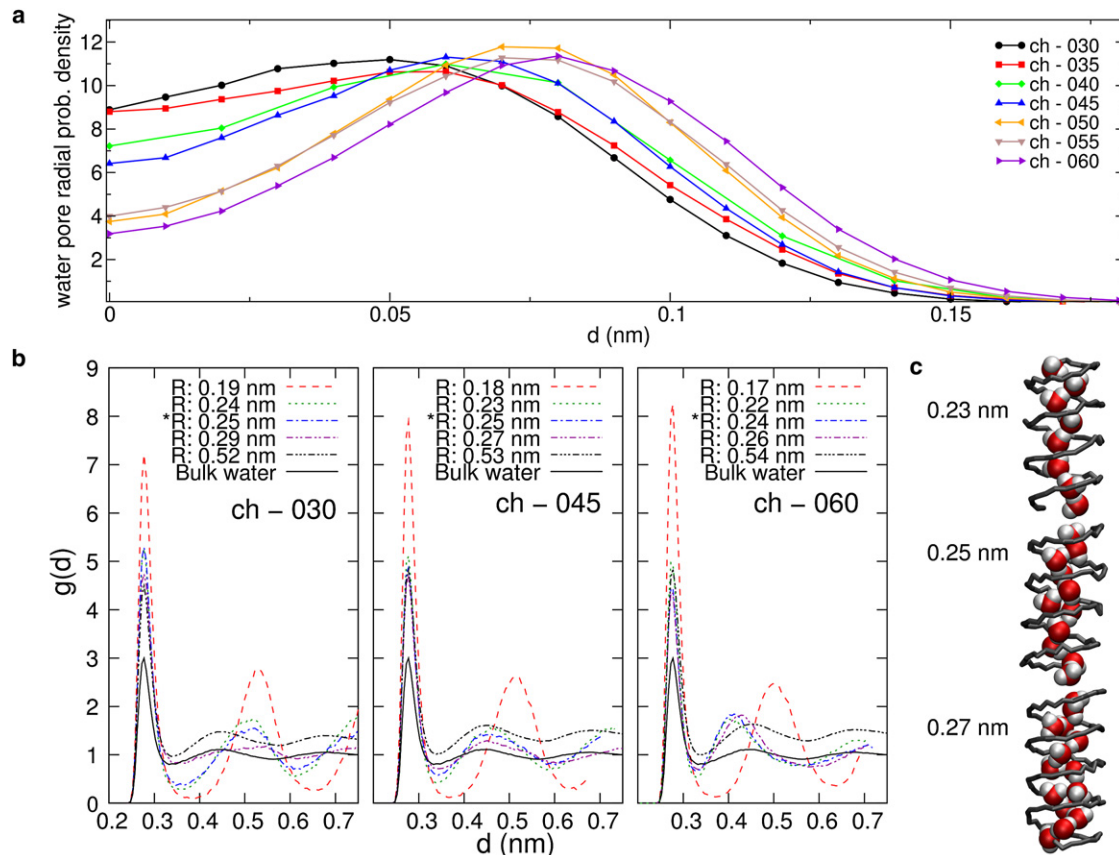


FIGURE 5 (a) Normalized radial probability density for channels of given pore radius ( $\sim 0.18$  nm) at different pore polarities. As the polarity of the pore increases the maximum of the probability density is shifted toward the wall of the pore. (b) Radial distribution function  $g(d)$  (RDF) for water molecules inside the pore as a function of the effective pore radius at three different pore polarities (ch-030, ch-045, and ch-060). The red curves show the radius corresponding to the highest water density. The green, blue, and magenta curves illustrate the transition from single-file to non single-file. The starred radius indicates the radius at which the transition occurs. The solid black curve indicates the RDF at the largest pore radius studied, which has the characteristic extrema pattern of bulk water (solid curve). (c) Illustration of the transition from the single-file regime (upper channel,  $R = 0.23$  nm) toward a double-file (lower channel,  $R = 0.27$  nm) for the ch-045 pore polarity.

the RDF at a radius where the double-file is the predominant configuration. Finally, the pattern of extrema at large radii (dashed-triple-dotted) is the same as in bulk water (black curve), although the absolute value of  $g(d)$  differs due to the confined geometry of the pore.

The change in position of the second peak is a robust indicator of the transition from and to a single-file in pores with low polarity. Because the water molecules tend to lie at the center of the pore in channels with low polarity, as seen in Fig. 5, the second peak is located very close to twice the water-water distance (0.55 nm). As the channel becomes more hydrophilic, the water molecules move toward the walls of the pore, thereby shifting the second maximum to shorter distances. For pores of higher polarity than ch-045 the transition becomes smoother in terms of the RDF.

### Permeability coefficients as function of the pore size and polarity

The thermodynamic properties presented in the previous section characterize the dependence of the pore occupancy

and the water structure as a function of the pore radius and polarity. In addition to these static features, we now focus on how the dynamics of the permeating water molecules depend on channel radius, length and polarity. To describe the mobility of water molecules inside the channel we used the osmotic and diffusive permeability coefficients.

Osmotic and diffusive permeability coefficients for the peptidic channels of three different lengths and seven different polarities are displayed in Fig. 6. The modulation of the polarity of the peptidic backbone results in a large variation of permeability coefficients, both osmotic and diffusive. Changing the dipole moment of the peptide backbone carbonyl groups from 1.72 D to 2.59 D increases the osmotic permeability coefficient  $\sim 5$ -fold. A further increase of pore polarity to 3.45 D decreases the osmotic permeability coefficients by roughly the same amount. These results agree very well with previous analytic models (52). The OPLS-AA charges, which closely mimic the polarity of naturally occurring amino acids, were found to be close to optimal for water permeation. The bell-shaped dependence of the osmotic and

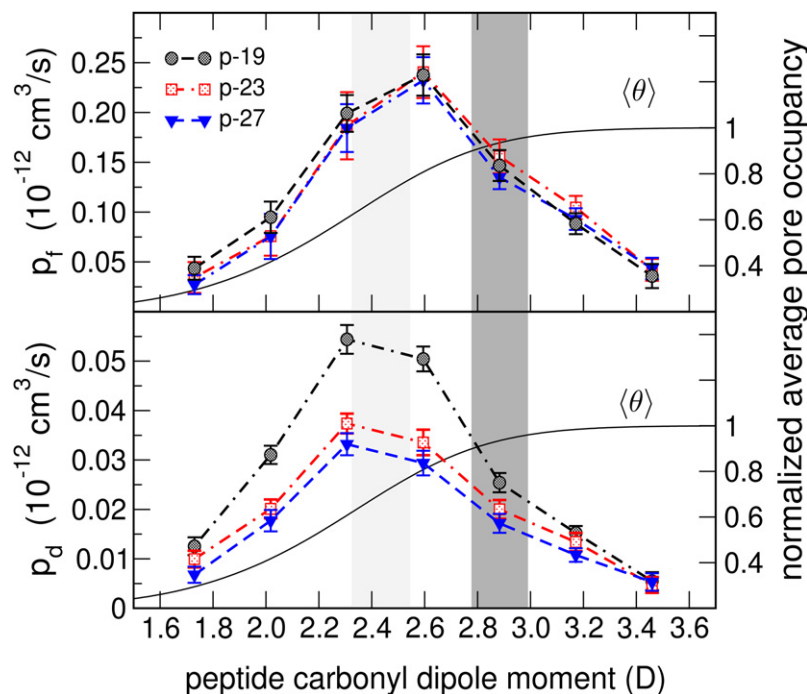


FIGURE 6 Osmotic,  $p_f$ , and diffusive,  $p_d$ , permeability coefficients as a function of the dipole moment of the peptide backbone carbonyl group for the three channels studied, averaged over two independent simulations for each polarity. The fitted averaged occupancy  $\langle \theta \rangle$  at each polarity is displayed as a continuous line. The light gray area indicates the polarity at which the permeability is the highest, correlated with intermediate backbone polarity and medium water occupancies. The dark gray indicates the dipole corresponding to the OPLS charges.

diffusive permeability coefficients can be explained by simple intuitive arguments, similar to the ones put forward by Chou (52): low polarities imply low occupancies, but fast fluxes once the water molecules are in the pore. Increasing the polarity raises the average occupancy allowing more molecules to permeate within a given time frame. A further increase of the water pore-affinity prevents fast hops of water molecules, and effectively reduces the water flux. Consequently, the maximum flux was found to be at intermediate pore affinities.

As observed previously for the OPLS-AA charges (17), the osmotic permeability coefficient is effectively independent of the length of the water column. Even though the behavior of water inside the pore changes with polarity, the mobility of the water molecules does not strongly depend on the length of the water column within the studied range of channel lengths. This finding is consistent with the computed normalized water occupancy as a function of the backbone polarity, which was also found to be independent of the channel length. The diffusive permeability coefficient, related to the number of water molecules that completely cross the pores, decreases as the channel length grows. Because the mobility of the water molecules in the channels of different length is the same at a given channel polarity, water molecules require longer times to completely translocate the channel, and therefore the channels present lower  $p_d$  values. The most significant difference occurs at intermediate polarities, analogous to the  $p_f$ , due to the greatest variation in mobility of the water molecules.

We have seen that slight modifications of the water-channel affinity can lead to substantial changes in the permeability of the channel. We will now see that also small

variations in the channel radius lead to large differences in water mobility, especially in the single-file regime. In this study, the pore radius is the only parameter that was varied given a channel polarity, and therefore is the independent variable. However, we have seen that the pore water occupancy and the pore water density are useful quantities to describe the system. We will therefore discuss the relationship between the permeability coefficients, the radius of the pore, and the average pore occupancy.

In Fig. 7, *a* and *b*, the osmotic ( $p_f$ ) and diffusive ( $p_d$ ) permeability coefficients as function of the pore radius for different pore polarities are shown. Fig. 7, *a'* and *b'* show  $p_f$  and  $p_d$  as function of the pore occupancy per nm. The rough global dependence of the permeability coefficients on the radius requires at least a polynomial of second order to be described, although close examination shows severe deviations (data not shown). The slope change of the osmotic permeability as a function of the radius indicates a transition between permeation regimes with changing radial dependence. For  $p_f$  there are three distinguishable regions of almost constant slope, which could all be well approximated by an exponential increase. Regrettably, there is no universal expression for the dependence of  $p_f$  with the radius that accounts for all regimes. The equation proposed by Longuet-Higgins and Finkelstein is only valid for single-file channels (13,53),

$$p_f = \frac{v_w D_w^0 N}{L^2}, \quad (3)$$

where  $v_w$  is the molar water volume,  $L$  is the length of the pore, and  $D_w^0$  is the average diffusivity a water molecule would have if it would be alone in the pore. The same holds

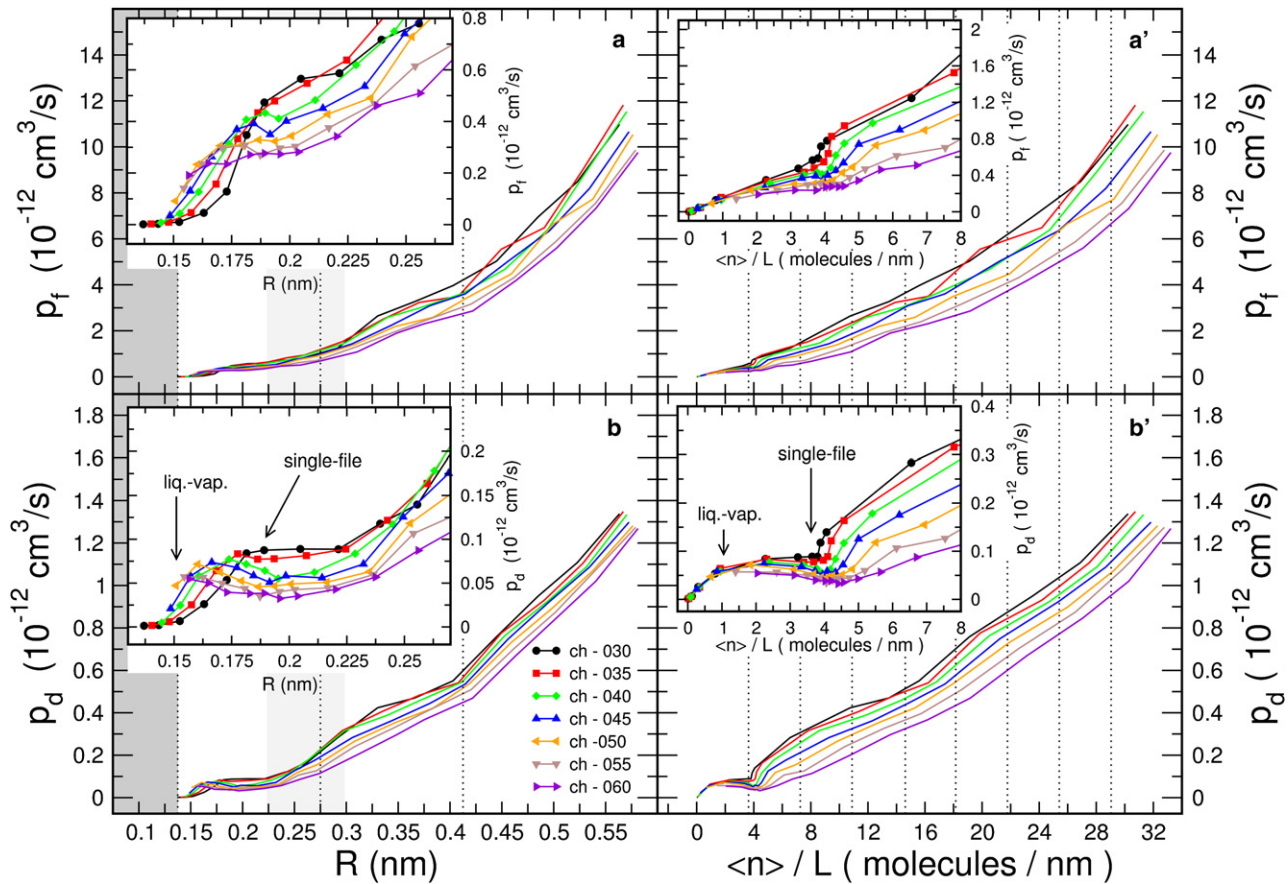


FIGURE 7 (a and b) Osmotic (upper left panel) and diffusive (lower left panel) permeability coefficients for different pore polarities as a function of the pore radius. (a' and b') Osmotic (upper right panel) and diffusive (lower right panel) permeability coefficients as a function of the pore water occupancy (divided by the length of the pore). The insets are detailed views of the permeability coefficients at small pore radii. The dark gray area indicates a radius smaller than the water molecule radius, and the light gray area is positioned at the transition from/to the single-file regime. The vertical dashed lines indicate radii corresponding to multiples of a water molecule radius for a and b, and multiples of 3.63 water molecules per nm in a' and b'. Error bars are not drawn for clarity, the uncertainty is  $<10\%$  of the permeability coefficient reported.

for  $p_d$ : relationships were derived for single-file and for macroscopic pores (13), but there are no general expressions for any value of  $R$ .

The mobility inside the channels with almost any radius  $>0.2$  nm is highest in the more hydrophobic channels. Below this radius, the permeability coefficients follow a behavior similar to the polarity dependence in the polyalanine channels (radius  $\sim 0.16$  nm): low polarity pores are characterized by low permeability coefficients due to the incomplete pore occupancy, and high polarity pores have low permeabilities due to the friction caused by the attraction to the channel. The permeability coefficients at  $\sim 0.16$  nm radius are in the same range ( $p_f \sim 1.5 \times 10^{-13} \text{ cm}^3/\text{s}$ ) as the peptidic polyalanine channels. Once the low polarity pores are filled completely with water molecules, at radii  $>0.2$  nm, their permeability coefficients are larger than the ones of the more polar channels, due to the lower friction between the permeating water molecules and the pore wall.

The osmotic permeability coefficients monotonically increase with the water pore occupancy and the radius. The

channels of low hydrophilicity display an almost linear increase of  $p_f$  with the occupancy until the configuration of maximally packed single-files is reached, in good agreement with the prediction of Eq. 3. The slope of the linear dependence of the  $p_f(N)$  curve is below one. This implies that, because the average occupancy reflects opening times, the increased frequency of open states lowers the rate at which the molecules permeate under an osmotic gradient (otherwise the slope of  $p_f(N)$  would have been one or larger). Nevertheless, because the channel is in the open state for longer periods, the overall osmotic permeability increases. Therefore, the regime connected to the liquid-vapor oscillations (burst-like behavior) does not necessarily imply fast permeations, as has been suggested (54).

At the highest density of the single-file there is a sudden increase of the osmotic permeability as a function of the radius in a very small range of pore occupancies. This effect is due to the steady expansion of available area with the radius in the transition from single-file configuration. In this study, the transition of the osmotic permeability

becomes smoother for the more hydrophilic pores, and for ch-060 it is almost linear. At an occupancy of  $\sim 5.6$  water molecules per nm, corresponding to the midpoint between single and double-file, the fast increase of  $p_f$  stops and remains growing linearly with the occupancy. As can be seen from Fig. 7 *d'*, the consecutive crossings of occupancy regimes (single, double, triple, etc.) increase the dependence of the  $p_f$  on the occupancy.

Whereas the  $p_f$  always increases with the radius, the diffusive permeability coefficient  $p_d$  shows a remarkably different behavior, especially in the single-file regime. All channels show an increase of the  $p_d$  with the pore occupancy at water pore densities lower than half the density of bulk water. In this pore range, the averaged occupancies reflect fractions of time in which the channels are open. Intermittent permeations of few water molecules contribute to the diffusive permeability, and therefore  $p_d$  increases with the fraction of open time, i.e., with the radius. For channels more polar than ch-030 there is a drop in the  $p_d$  for radii larger than the radius for which the single-file regime is well-defined. For ch-030 there is no decrease in the diffusive flux at this radius, but it remains almost constant. Once the radius of a hydrophilic channel is large enough to form a single-file configuration with a probability  $>50\%$ , the  $p_d$  starts decreasing when increasing the radius further. The low diffusion constant of the single file regime with respect to the bulk water is a characteristic behavior (23,55,56). The results of this work show that the decay of the diffusive permeability with the radius is characteristic of hydrophilic pores before the single-file configuration is reached. In the simulations presented by Beckstein et al. (30), the reported equilibrium diffusive flux as a function of the pore radius in a completely hydrophobic pore presents no reduction of diffusive flux, in agreement with our results and interpretations. At a pore radius larger than  $\sim 0.2$  nm the pore density decreases significantly and the water diffusivity starts increasing due to the larger volume available. To a lesser extent, the attenuation of  $p_d$  is also visible at the radius corresponding to the establishment of the triple-file regime ( $\sim 0.32$  nm), a local maximum for the less polar channels.

To further rationalize the decrease of the diffusive flux with the radius in the hydrophilic pores, consider the average water density in the channel (Fig. 4 *c*) and the distribution of pore occupancies over the simulation time, which are analogous to the one presented for polyalanine channels (Fig. 3). For pores with a water density less than half the bulk density, corresponding to an average occupancy of 1.8 water molecules per nm, the behavior of water molecules in the pores is characterized by so-called liquid-vapor oscillations (27). Water molecules permeating the channel do so in small clusters, and the averaged occupancy reflects fractions of time in which the pore is open, i.e., proportional to  $p_d$ . The diffusive permeability of ch-030 does not decrease with increasing radius because, even at the highest density, the channel is still characterized by a significant contribution from empty

states. After the averaged density reaches  $0.5 \rho_0$ , the dominant contribution is from the single-file, and therefore the diffusion permeability suffers a decrease due to the lower diffusivity of the single-file configuration as compared to individual water molecules or small clusters (55,56,23). Highly hydrophobic channels do not show the decrease in the diffusive permeability because the liquid state is only stable at large radii, where the single-file configuration does not contribute significantly.

### Hydrophilicity and osmotic permeability coefficients of peptidic and proteic single-file channels

To compare the hydrophilicity of our model channels with natural or synthetic single-file channels we used the water density inside the channel, normalized to the density of bulk water. The water density inside the channels reflects both the energetic and the entropic contributions that define the hydrophilicity.

We computed the averaged normalized water density in the single-file region of gramicidin A (gA), midgramicidin (MDg), Aquaporin 1 (Aqp-1) and Glycerol Facilitator (GlpF), and we found very similar values (Table 1). Whereas all model channels studied in this study have regular structures of well defined geometry, Aquaporins form a large family of water conducting membrane proteins with subtle but important structural variations. These proteins are endowed with heterogeneously decorated water pathways, with varying radii along the channel. It is therefore difficult to assess the specific weight of a given geometric or electrostatic property on the observed permeability coefficients. The experimental single-channel osmotic permeability coefficients for Aqp-1 (average radii in the single-file region  $\sim 0.16$  nm, normalized water density 1.34) is  $5.4 \times 10^{-14}$  cm<sup>3</sup>/s, whereas for GlpF (averaged radius  $\sim 0.19$ , normalized water density 1.25), the reported experimental value is  $0.7 \times 10^{-14}$  cm<sup>3</sup>/s. The latest value is however found to be an order

**TABLE 1** Osmotic permeability coefficient ( $p_f$ ), effective pore radii ( $R_{\text{eff}}$ ), and pore water density, for different single-file conducting water channels

Channel	$p_f$ ( $10^{-14}$ cm <sup>3</sup> /s)	$R_{\text{eff}}$ (nm)	$\rho_{\text{pore}}/\rho_{\text{bulk}}$
p-ala ( $D = 2.88$ )	15 (sim.)	0.14	1.26
model (ch 060)	23 (sim.)	0.16	1.21
gA	1.6 (exp (63).)	0.14	1.28
MDg	5.6 (exp (16).)	0.15	1.20
Aqp-1	5.4 (exp (64).)	0.16	1.34
GlpF	0.7 (exp (65).)	0.19	1.25
	$\sim 14$ (sim (57–59).)		

The water density is normalized to the water density of bulk water ( $\rho_{\text{pore}}/\rho_{\text{bulk}}$ ). Reference to permeability coefficients not obtained from this work are given in parenthesis, specifying whether the measurement is experimental (exp.) or from molecular dynamics simulations (sim.) Effective pore radii and water density were extracted from atomistic molecular dynamics simulations. See Supporting Material for details and normalized pore water density for all the studied polyalanine channels.

of magnitude larger ( $\sim 1.4 \times 10^{-13} \text{ cm}^3/\text{s}$ ) in multiple simulations studies (57–59). Although not attributed to the difference in radii (16), the less hydrophilic and slightly wider pore of MDg permeates water at much faster rates than gA.

Because we use position restraints to keep the channel fixed around highly permeable conformations and we avoid membrane-channel disturbances, the permeability coefficients computed for our model channels are in general an order of magnitude larger than typical values for gramicidin A and aquaporins.

### The ratio of $p_f$ to $p_d$ and the proportionality to the pore water occupancy

One of the most celebrated equalities in the framework of single-file transport is the ratio of osmotic and diffusive permeability, which equals to the number of water molecules ( $n$ ) that fit in the channel (13,60). The generally accepted result is  $p_f/p_d = n + 1$  (17,24,48,61,62), which has been derived by means of several formalisms. In the mechanistic view of water molecules jumping from binding site to binding site, the  $n + 1$  factor results from the fact that it takes  $n + 1$  jumps across  $n$  water positions to fully cross the channel. The frequency of water jumps by one water-water distance are proportional to  $p_f$ , and the number of complete water translocations is proportional to  $p_d$ .

Fig. 8 shows the ratio of osmotic permeabilities ( $-1$ ) as a function of the averaged pore occupancy. The straight black line represents the  $p_f/p_d = n + 1$  result. As can be seen, the prediction of the occupancy is fulfilled for all channels and polarities. The highest (but insignificant) deviations from the  $\langle n \rangle + 1$  ratio occur at high and very low polarities, which can be attributed to the low number of water passage under these conditions. This remarkable finding shows that the  $p_f/p_d = n + 1$  relationship also holds for partially filled channels, when  $n$  is replaced by  $\langle n \rangle$ . The ratio of osmotic and diffusive permeabilities should therefore be expressed as

$$\frac{p_f}{p_d} = \langle n \rangle + 1, \quad (4)$$

implying that it captures the averaged occupancy. This result has an important implication: it allows the experimental detection of liquid-vapor oscillations in single-file channels. Occupancies can be computed by measuring the averaged number of water molecules using  $p_f/p_d = n + 1$ , and the degree of occupancy on the maximum number of water molecules that geometrically fit in the single-file pore. If the channel shows strong occupancy fluctuations, the observed permeability ratio would be significantly smaller than the maximum occupancy allowed by the channel length.

To expand the study of the validity of Eq. 4, especially in the transition from the single-file to double-file regime, we will characterize the ratio of permeability coefficients for pores of different radius and polarity. Fig. 9 a shows a combined representation of averaged pore water occupancies and the

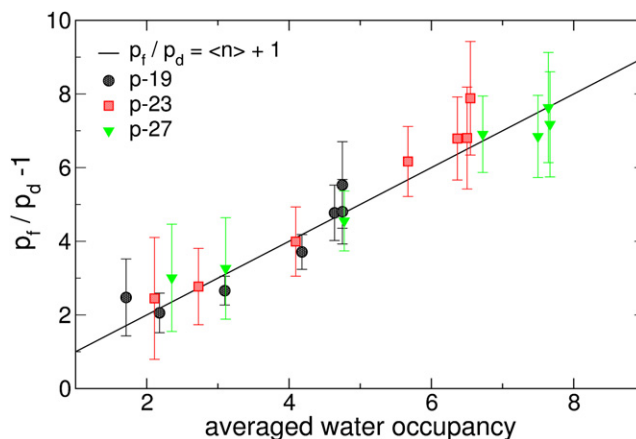


FIGURE 8 The ratio of osmotic and diffusive permeation coefficients for the set  $p_f/p_d$ , is linearly proportional to the averaged water occupancy in the single-file peptidic pores for any peptide backbone polarity.

ratio of permeability coefficients as a function of the pore radius. The ratio of permeability coefficients is in good agreement with Eq. 4 in the whole range of radii in the single-file region. The outlier ch-030 at  $R = 0.12 \text{ nm}$  is most likely due to limited statistics for  $p_d$  and  $\langle n \rangle$  for this very narrow channel. The two curves drift apart at values of the radius that correlate with the structural or thermodynamic indicators used in this work, the local minimum in the water pore density as a function of the radius and the second maximum in the RDF. In this sense, the ratio of  $p_f$  and  $p_d$  is another indicator of the transition from the single-file regime. Although the significance of  $p_f/p_d$  is clear in the single-file transport, its value beyond that regime is not known. More precisely, it is not known which is the dependence with the radius in the interval between single-file and macroscopic pore (13). We show that after crossing the single-file regime, the ratio decays to a local minimum, correlating with the increase in water pore density. At a radius of  $0.35 \text{ nm}$ , the ratio remains almost constant until  $\sim 0.45 \text{ nm}$ , where a trend toward higher values starts.

Dividing the averaged pore occupancy by  $(p_f/p_d - 1)$  clearly yields one in the single-file regime. If the permeation mainly occurs via independent single-file like structures embedded in the channel, the ratio is expected to be directly proportional to the averaged occupancy at the single-file regime. Fig. 9 b shows the value of  $(\langle n \rangle + 1)/(p_f/p_d)$  as a function of the radius. The single-file regime is indeed characterized by a value of one, and the potential changes of file regimes are indicated by crossings of integer values of the abscissa. Fig. 9 c shows the correlation between the computed  $(\langle n \rangle + 1)/(p_f/p_d)$  and the expected value based on the averaged occupancies. To determine the number of single-file columns per nanometer, the typical water-water distance is used ( $d_{\text{ww}} = 0.275 \text{ nm}$ ). The agreement between  $(\langle n \rangle + 1)/(p_f/p_d)$  and  $(\langle n \rangle/L)d_{\text{ww}}$  is remarkably good: deviations occur at the occupancies that correspond to the minima in the water pore density and in the large radius, where the liquid structure of the pore water converges to one of bulk

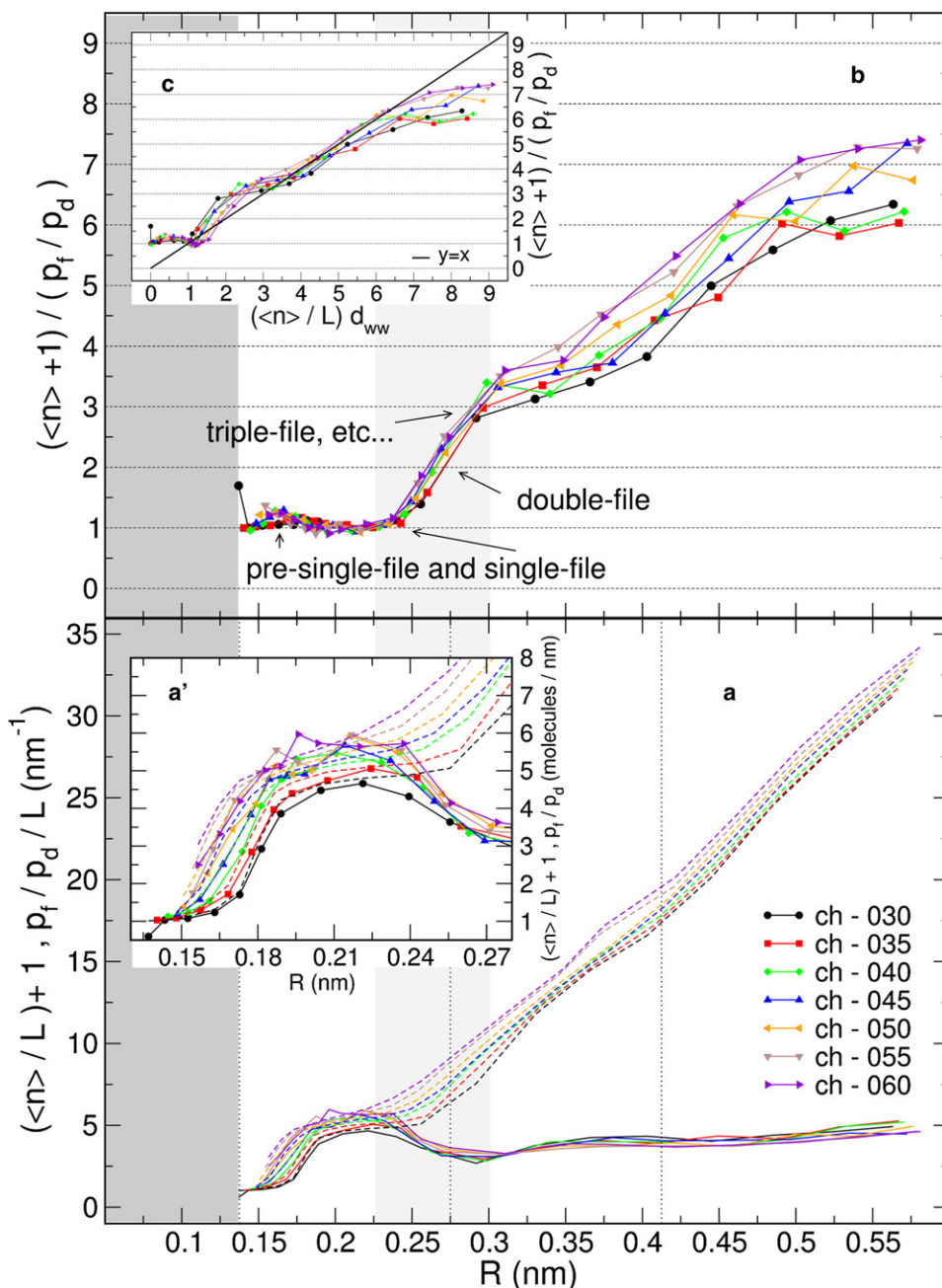


FIGURE 9 (a) Ratio of osmotic permeability coefficients,  $p_f/p_d$  (solid lines), and averaged pore water occupancy plus one (dashed lines) as function of pore radius. Both dependent variables were normalized by the length of the pore. The inset (a') focuses on the range of radii smaller than the diameter of a water molecule. The dark gray area indicates radius smaller than the radius of a water molecule, and the light gray area indicates the transition involving the single-file regime. (b) Ratio of  $(\langle n \rangle + 1)$  to  $(p_f/p_d)$  as function of the radius. (c) Correlation between  $(\langle n \rangle + 1)/(p_f/p_d)$  and  $(\langle n \rangle/L)d_{ww}$ , where  $d_{ww}$  is the typical water-water distance, established to 0.275 nm. Disregarding the radius where the pore presents a local minimum in the water density and radii  $>0.45$  nm, the ratio of occupancies and permeability coefficients correctly identifies the transitions between different file regimes. The solid line indicates  $(\langle n \rangle + 1)/(p_f/p_d) = (\langle n \rangle + 1)/(p_f/p_d)$ .

water. Because only the displacements along the pore axis contribute to the diffusive permeability, this result indicates that the relevant motions along the pore main axis effectively take place within single-files.

## CONCLUSIONS

We presented a detailed study of the influence of the pore size and the polarity of narrow hydrophilic pores on the water permeation. The structural and dynamical information obtained complements and expands the knowledge of the structure-activity relationship in water channels, which is valuable to understand the permeation mechanism of natu-

rally occurring channels and to design channels of desired properties. We believe that these results are useful to predict the response in the channel flux to changes in the concentration gradient between the solutions at each end of the channel, or which radius and polarity would allow a fast flux of water molecules while preserving the single-file regime. Because single-file channels are generally a requirement for the selectivity toward different solutes, we therefore paid special attention to this permeation regime.

The time-averaged pore occupancy as a function of pore polarity in peptidic single-file channels was found to follow a sigmoidal curve, which could be described by an equilibrium between occupied and unoccupied positions. At low

polarities we observed strongly fluctuating water occupancies in the pore, leading to broad distributions of the number of water molecules inside the channel. Moving toward high polarities raises the water occupancy and narrows the distribution of the number of water molecules inside the pore. The analysis of the pore water density showed characteristic oscillations in channels of radii smaller than three times the radius of a water molecule. Before the establishment of an uninterrupted flow of water molecules, on average at a radius of  $\sim 0.17$  nm, the density fluctuations can be well described by a liquid-vapor equilibrium (27). A perfectly packed single-file configuration presents a local maximum in the pore water density as a function of the pore radius, followed by a local minimum indicating the transition to a double-file regime. The polarity of the channel scales the water pore density: an increase in hydrophilicity of the pore leads to a corresponding increase of the pore water density, and modulates at which radius the transitions between different regimes takes place. At large pore radii, all water pore densities converge to the bulk density, and therefore the pore occupancy directly scales with the area and length of the pore. The changes in the structural arrangement from/to the no-pass regime can be followed by means of a radial distribution function: the intensity and position of the second maxima in the RDF indicate the dependence of the confinement of water molecules on the pore radius and polarity.

We showed that the pore polarity strongly affects the permeation coefficients, whereas the effect of the length was not found to be significant. In the single-file regime, the osmotic permeability always increases with the pore radius, scaling linearly with the pore occupancy until the densest single-file configuration is achieved. On the contrary, the diffusive permeability experiences a local maximum at radii where the density fluctuations average to half the bulk water density, and falls to a local minimum at the densest single-file configuration. Along with the transition from single-file to double-file, both the osmotic and diffusive permeability coefficients increase with the radius.

The ratio of osmotic and diffusive permeability coefficients was found to equal the averaged pore occupancy ( $+1$ ) for all pore polarities and radii that guarantee a no-pass condition, which can be used to experimentally identify liquid-vapor fluctuations in single-file channels. Beyond this single-file arrangement, the value of  $(p_i/p_d - 1)$  remains almost constant, equal to the occupancy corresponding to the densely packed single-file configuration. This implies that the confinement of the water molecules preserves the collective motions of water chains, effectively acting like single-files in parallel. As the channel becomes much wider, the ratios converge toward their expected macroscopic radial dependence.

For the design of new water channels, we have seen that the radius and polarity play a major role in determining the flow of water molecules, in contrast to the channel length, which has almost no impact on the osmotic permeability. In general, if the selectivity of the pore is not an issue, wide apolar channels

are the most effective in conducting a water flux. If we are constrained to the narrow single-file regime, less hydrophilic channels allow the single-file to persist at a larger radius than highly polar channels, and with faster rates.

## SUPPORTING MATERIAL

Water densities for the polyaniline channels and details on the gramicidin and aquaporin simulations are available at [http://www.biophysj.org/biophysj/supplemental/S0006-3495\(08\)00443-8](http://www.biophysj.org/biophysj/supplemental/S0006-3495(08)00443-8).

We thank Camilo Andrés Aponte-Santamaría for fruitful discussions and, together with Jochen S. Hub, for providing us with water density estimates for Aqp-1 and GlpF.

This study was supported by Deutsche Forschungsgemeinschaft grant GR-2079/2 (G.P.).

## REFERENCES

1. Agre, P. 2004. Aquaporin water channels (Nobel Lecture). *Angew. Chem. Int. Ed.* 43:4278–4290.
2. Jensen, P.H., and D. Keller. 2006. Membrane for filtering of water. Patent number WO 2006/122566.
3. Cornell, B. A., V. L. Braach-Maksvytis, L. G. King, P. D. Osman, B. Raguse, et al. 1997. A biosensor that uses ion-channel switches. *Nature*. 387:580–583.
4. Hirano, A., M. Wakabayashi, Y. Matsuno, and M. Sugawara. 2003. A single-channel sensor based on gramicidin controlled by molecular recognition at bilayer lipid membranes containing receptor. *Biosens. Bioelectron.* 18:973–983.
5. Futaki, S., Y. J. Zhang, T. Kiwada, I. Nakase, T. Yagami, et al. 2004. Gramicidin-based channel systems for the detection of protein-ligand interaction. *Bioorg. Med. Chem.* 12:1343–1350.
6. Borisenko, V., Z. Zhang, and G. A. Woolley. 2002. Gramicidin derivatives as membrane-based pH sensors. *Biochim. Biophys. Acta.* 1558:26–33.
7. Koeppe, R. E., and O. S. Anderson. 1996. Engineering the gramicidin channel. *Annu. Rev. Biophys. Biomol. Struct.* 25:231–258.
8. Banghart, M. R., M. Volgraf, and D. Trauner. 2006. Engineering light-gated ion channels. *Biochemistry*. 45:15129–15141.
9. Ghadiri, M. R., J. R. Granja, R. A. Milligan, D. E. McRee, and N. Khazanovich. 1993. Self-assembling organic nanotubes based on a cyclic peptide architecture. *Nature*. 366:324–327.
10. Ghadiri, M. R., J. R. Granja, and L. K. Buehler. 1994. Artificial transmembrane ion channels from self-assembling peptide nanotubes. *Nature*. 369:301–304.
11. Motesharei, K., and M. Ghadiri. 1997. Diffusion-limited size-selective ion sensing based on SAM-supported peptide nanotubes. *J. Am. Chem. Soc.* 119:11306–11312.
12. Braha, O., B. Walker, S. Cheley, J. J. Kasianowicz, L. Song, et al. 1997. Designed protein pores as components for biosensors. *Chem. Biol.* 4:497–505.
13. Finkelstein, A. 1987. Water Movement Through Lipid Bilayers, Pores, and Plasma Membranes. Wiley & Sons, New York.
14. Pappenheimer, J. R. 1953. Passage of molecules through capillary walls. *Physiol. Rev.* 33:387–432.
15. Paganelli, C. V., and A. K. Solomon. 1957. The rate of exchange of tritiated water across the human red cell membrane. *J. Gen. Physiol.* 41:259–277.
16. Saparov, S. M., J. R. Pfeifer, L. Al-Momani, G. Portella, B. L. de Groot, et al. 2006. Mobility of a one-dimensional confined file of water molecules as a function of file length. *Phys. Rev. Lett.* 96:148101.
17. Portella, G., P. Pohl, and B. L. de Groot. 2007. Invariance of single-file water mobility in gramicidin-like peptidic pores as function of pore length. *Biophys. J.* 92:3930–3937.

18. Levitt, D. G. 1973. Dynamics of a single-file pore: non-Fickian behavior. *Phys. Rev. A*. 8:3050–3054.
19. Richards, P. M. 1977. Theory of one-dimensional hopping conductivity and diffusion. *Phys. Rev. B*. 16:1393–1409.
20. Alexander, S., and P. Pincus. 1978. Diffusion of labeled particles on one-dimensional chains. *Phys. Rev. B*. 18:2011–2012.
21. Fedders, P. A. 1978. Two-point correlation functions for a distinguishable particle hopping on a uniform one-dimensional chain. *Phys. Rev. B*. 17:40–46.
22. Levitt, D. G. 1973. Kinetics of diffusion and convection in 3.2 Å pores. *Biophys. J.* 13:186–206.
23. Allen, T., S. Kuyucak, and S. H. Chung. 1999. The effect of hydrophobic and hydrophilic channel walls on the structure and diffusion of water and ions. *J. Chem. Phys.* 111:7985–7999.
24. Hummer, G., J. C. Rasaiah, and J. P. Noworyta. 2001. Water conduction through the hydrophobic channel of a carbon nanotube. *Nature*. 414:188–190.
25. de Groot, B. L., D. P. Tieleman, P. Pohl, and H. Grubmüller. 2002. Water permeation through gramicidin A: desformylation and the double helix; a molecular dynamics study. *Biophys. J.* 82:2934–2942.
26. Allen, R., S. Melchionna, and J. P. Hansen. 2002. Intermittent permeation of cylindrical nanopores by water. *Phys. Rev. Lett.* 89:175502.
27. Beckstein, O., and M. S. Sansom. 2003. Liquid-vapor oscillations of water in hydrophobic nanopores. *Proc. Natl. Acad. Sci. USA*. 100:7063–7068.
28. Kalra, A., S. Garde, and G. Hummer. 2003. Osmotic water transport through carbon nanotube membranes. *Proc. Natl. Acad. Sci. USA*. 100:10175–10180.
29. Tarek, M., B. Maigret, and C. Chipot. 2003. Molecular dynamics investigation of an oriented cyclic peptide nanotube in DMPC bilayers. *Biophys. J.* 85:2287–2298.
30. Beckstein, O., and M. S. P. Sansom. 2004. The influence of geometry, surface character, and flexibility on the permeation of ions and water through biological pores. *Phys. Biol.* 1:42–52.
31. Rasaiah, J. C., S. Garde, and G. Hummer. 2008. Water in nonpolar confinement: from nanotubes to proteins and beyond. *Annu. Rev. Phys. Chem.* 59:713–740.
32. Fang, H., R. Wan, X. Gong, H. Lu, and S. Li. 2008. Dynamics of single-file water chains inside nanoscale channels: physics, biological significance and applications. *J. Phys. D Appl. Phys.* 41:103002.
33. Dzubiella, J., and J. -P. Hansen. 2005. Electric-field-controlled water and ion permeation of a hydrophobic nanopore. *J. Chem. Phys.* 122:234706.
34. Freitas, J. A., D. J. Tobias, and S. H. White. 2006. A voltage-sensor water pore. *Biophys. J.* 91:L90–L92.
35. Li, J., X. Gong, H. Lu, D. Li, H. Fang, et al. 2007. Electrostatic gating of a nanometer water channel. *Proc. Natl. Acad. Sci. USA*. 104:3687–3692.
36. Kaminski, G. A., R. A. Friesner, J. Tirado-Rives, and W. L. Jorgensen. 2001. Evaluation and reparametrization of the OPLS-AA force field for proteins via comparison with accurate quantum chemical calculations on peptides. *J. Phys. Chem. B*. 105:6474–6487.
37. Jorgensen, W. L., D. S. Maxwell, and J. Tirado-Rives. 1996. Development and testing of the OPLS All-atom force field on conformational energetics and properties of organic liquids. *J. Am. Chem. Soc.* 118:11225–11236.
38. Jorgensen, W. L., J. Chandrasekhar, J. D. Madura, R. W. Impey, and M. L. Klein. 1983. Comparison of simple potential functions for simulating liquid water. *J. Chem. Phys.* 79:926–935.
39. Lindahl, E., B. Hess, and D. Van der Spoel. 2001. GROMACS 3.0: a package for molecular simulation and trajectory analysis. *J. Mol. Model.* 7:306–317.
40. Van der Spoel, D., E. Lindahl, B. Hess, G. Groenhof, A. E. Mark, et al. 2005. GROMACS: fast, flexible and free. *J. Comput. Chem.* 26:1701–1718.
41. Darden, T., D. York, and L. Pedersen. 1993. Particle mesh Ewald: an N·log(N) method for Ewald sums in large systems. *J. Chem. Phys.* 98:10089–10092.
42. Essmann, U., L. Perera, M. L. Berkowitz, T. Darden, H. Lee, et al. 1995. A smooth particle mesh Ewald potential. *J. Chem. Phys.* 103:8577–8592.
43. Miyamoto, S., and P. A. Kollman. 1992. SETTLE: an analytical version of the SHAKE and RATTLE algorithms for rigid water models. *J. Comput. Chem.* 13:952–962.
44. Hess, B., H. Bekker, H. J. C. Berendsen, and J. G. E. M. Fraaije. 1997. LINCS: a linear constraint solver for molecular simulations. *J. Comput. Chem.* 18:1463–1472.
45. Berendsen, H. J. C., J. P. M. Postma, A. DiNola, and J. R. Haak. 1984. Molecular dynamics with coupling to an external bath. *J. Chem. Phys.* 81:3684–3690.
46. Smart, O. S., J. G. Neduvellil, X. Wang, B. A. Wallace, and M. S. P. Sansom. 1996. HOLE: a program for the analysis of the pore dimensions of ion channel structural models. *J. Mol. Graph.* 14:354–360.
47. de Groot, B. L., and H. Grubmüller. 2005. The dynamics and energetics of water permeation and proton exclusion in aquaporins. *Curr. Opin. Struct. Biol.* 15:176–183.
48. Zhu, F., E. Tajkhorshid, and K. Schulten. 2004. Theory and simulation of water permeation in aquaporin-1. *Biophys. J.* 86:50–57.
49. Zhu, F., E. Tajkhorshid, and K. Schulten. 2004. Collective diffusion model for water permeation through microscopic channels. *Phys. Rev. Lett.* 93:224501.
50. Beckstein, O., K. Tai, and M. S. P. Sansom. 2004. Not ions alone: barriers to ion permeation in nanopores and channels. *J. Am. Chem. Soc.* 126:14694–14695.
51. Noon, W. H., K. D. Aumann, R. E. Smalley, and J. Ma. 2002. Helical ice-sheets inside carbon nanotubes in the physiological condition. *Chem. Phys. Lett.* 355:445–448.
52. Chou, T. 1998. How fast do fluids squeeze through microscopic single-file pores? *Phys. Rev. Lett.* 80:85–88.
53. Longuet-Higgins, H. C., and G. Austin. 1966. The kinetics of osmotic transport through pores of molecular dimensions. *Biophys. J.* 6:217–224.
54. Saparov, S. M., and P. Pohl. 2004. Beyond the diffusion limit: Water flow through the empty bacterial potassium channel. *Proc. Natl. Acad. Sci. USA*. 101:4805–4809.
55. Dani, J. A., and D. G. Levitt. 1981. Water transport and ion-water interaction in the gramicidin channel. *Biophys. J.* 35:501–508.
56. Hahn, K., J. Kärger, and V. V. Kukla. 1996. Single-file diffusion observation. *Phys. Rev. Lett.* 76:2762–2765.
57. Zhu, F., E. Tajkhorshid, and K. Schulten. 2002. Pressure-induced water transport in membrane channels studied by molecular dynamics. *Biophys. J.* 83:154–160.
58. Hashido, M., M. Ikeguchi, and A. Kidera. 2005. Comparative simulations of aquaporin family: AQP1, AQPZ, AQP0 and GlpF. *FEBS Lett.* 579:5549–5552.
59. Jensen, M. Ø., and O. G. Mouritsen. 2006. Single-channel water permeabilities of *Escherichia coli* aquaporins AqpZ and GlpF. *Biophys. J.* 90:2270–2284.
60. Levitt, D. G. 1974. A new theory of transport for cell membrane pores. I. General theory and application to red cell. *Biochim. Biophys. Acta.* 373:115–131.
61. Hernandez, J. A., and J. Fischbarg. 1992. Kinetic analysis of water transport through a single-file pore. *J. Gen. Physiol.* 99:645–662.
62. Berezhkovskii, A., and G. Hummer. 2002. Single-file transport of water molecules through a carbon nanotube. *Phys. Rev. Lett.* 89:064503.
63. Pohl, P., and S. M. Saparov. 2000. Solvent drag across gramicidin channels demonstrated by microelectrodes. *Biophys. J.* 78:2426–2434.
64. Engel, A., and H. Stahlberg. 2002. Aquaglyceroporins: Channel Proteins with a Conserved Core, Multiple Functions and Variable Surfaces., Vol. 215. International Review of Cytology. Academic Press, New York., 75–104.
65. Saparov, S. M., S. P. Tsunoda, and P. Pohl. 2005. Proton exclusion by an aquaglyceroprotein: a voltage clamp study. *Biol. Cell.* 97:545–550.